RSC Advances

PAPER

View Article Online
View Journal | View Issue

Cite this: *RSC Adv.*, 2017, **7**, 50966

A general synthesis of abundant metal nanoparticles functionalized mesoporous graphitized carbon†

Tao Wang,[a] Yan Sun,[a] Ang Li,[a] Yali Ma,[a] Danyang Feng,[a] Youxing Fang,[b] Yunling Liu,[a] Qisheng Huo,[a] Zhen-An Qiao*[a] and Sheng Dai[c]

Received 29th August 2017
Accepted 16th October 2017

DOI: 10.1039/c7ra09560k

rsc.li/rsc-advances

The abundant transition metal and carbon sources allow imaginative combinations to design porous functional metal–carbon composites for wide applications. However, cumbersome and restricted methods seriously limit the development of mesoporous metal–carbon composites. In this study, a general coordination–polymerization method is reported to construct metal–gallic acid resin, and mesoporous carbon with highly dispersed metal nanoparticles and high metal nanoparticle concentration up to 20 wt%. The metal element composited with polymer and carbon can be various transition metals containing Ti, V, Cr, Mn, Fe, Co, Ni, Cu, and Zn. Furthermore, the general strategy can be expanded to the fabrication of N doped bimetallic catalyst FeCo–MCN-900, which shows comparable electrocatalytic activity and higher stability compared to commercial Pt/C.

1. Introduction

The development of society is heavily dependent on energy conversion and storage.[1,2] As potential power sources, fuel cells powered by hydrogen from secure and renewable sources are the ideal solution for non-polluting vehicles, but demand highly efficient catalysts for anodic and cathodic reactions.[3–7] Though Pt and its alloy meet the requirement of high activity, poor long-term duration and low abundant of Pt in nature restrict the practical large-scale commercialization of fuel cells.[6,8–11] Scientists have invested much time and energy in getting candidates for Pt, such as non-precious-metal catalysts and metal free heteroatom-doped carbon materials.[12–20] It is noteworthy that the abundant transition metal and carbon sources allow imaginative combinations to form porous functional metal–carbon composites and show comparable activity as commercial Pt/C catalyst.[21–29] For example, He's group reported a hybrid material (Co–W–C/N) with tungsten carbide and cobalt nanoparticles encapsulated in an N-doped porous carbon framework, which exhibited excellent electrocatalytic activity and high stability.[30] Mesoporous carbons (MCs) derived from polymers are a class of vibrant support materials that combine efficient mass transfer efficiency with good electrical conductivity.[31–35] MCs with the critical sites such as metal nanoparticles and pyridinic N have been reported as efficient catalysts.[36–44] There is still a problem in the reconciliation of high metal content (>10 wt%) and highly dispersed metal nanoparticles (<100 nm) supported by carbon materials. To this end, metal–ligand coordination materials including metal–organic frameworks (MOFs) and amorphous coordination compounds constructed by metal (clusters) and carboxylate or/and N-involved ligand with huge diversity and uniform heteroatom decoration, intuitively should be a class of available precursors to produce metal-rich carbon catalysts.[22,36–44] However, the poor thermal stability of coordination materials generally leads to the failure of the conversion to metal-rich carbon catalysts.[37,41,45] How to stabilize coordination materials is still a burning question that waiting for a new and effective solution.

Merging concepts and tools from different methodologies is an important approach to develop defined functional materials targeting selected applications. Herein, we reported a general coordination–polymerization strategy combining flexible coordination mode with stable polymer network to construct metal–gallic acid resin (X–GR) and mesoporous carbon materials with high metal nanoparticle concentration as efficient ORR catalysts. As shown in Fig. 1a, gallic acid (GA) and Fe^{III} were typically chosen as the organic ligand and the metal ions to form iron gallate (Fe–GA) nanoparticles at certain pH value. The coordination Fe–GA was further crosslinked by the polymerization of GA with formaldehyde to obtain iron gallate resin (Fe–GR). Fe–mesoporous carbon (Fe–MC) with dispersed Fe_3C nanoparticles

[a]State Key Laboratory of Inorganic Synthesis and Preparative Chemistry, Jilin University, Changchun, Jilin 130012, China. E-mail: qiaozhenan@jlu.edu.cn
[b]State Key Laboratory of Electroanalytical Chemistry, Changchun Institute of Applied Chemistry, Chinese Academy of Science, 5625 Renmin Street, Changchun, Jilin 130022, China
[c]Chemical Sciences Division, Oak Ridge National Laboratory, Oak Ridge, TN 37831, USA

† Electronic supplementary information (ESI) available: SEM images of X–GR, TG curves of Fe–GA and Fe–GR, pore size distribution analysis for Fe–MC-*x*, N_2 adsorption–desorption isotherms of X–MC-600, PXRD patterns of X–MC-*x*, characterizations of FeCo–MCN-900. See DOI: 10.1039/c7ra09560k

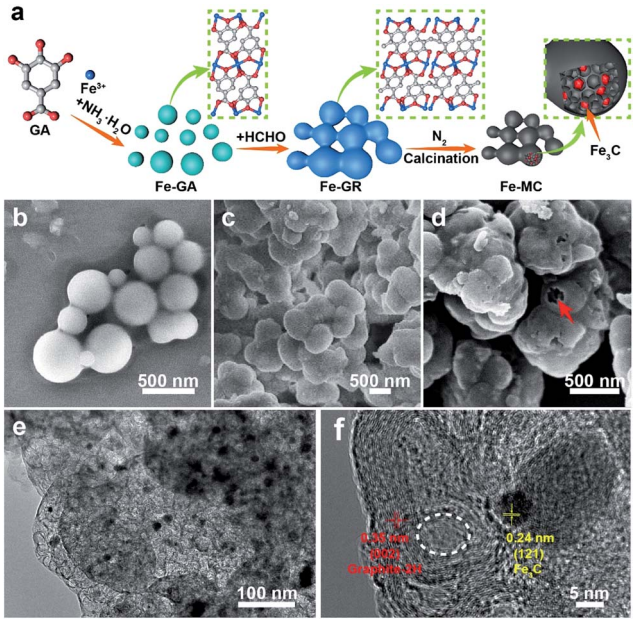

Fig. 1 (a) Schematic illustration of the synthetic process of Fe–GA, Fe–GR and Fe–MC. SEM images of Fe–GA (b), Fe–GR (c) and Fe–MC (d). The arrow in panel c showing a broken sphere. (e) TEM image of Fe–MC. (f) HRTEM image of Fe–MC. The dotted circle in panel (f) showing a hole about 10 nm width.

about 20 nm was obtained by the carbonization of Fe–GR under nitrogen atmosphere. The Fe content of Fe–MC are calculated to be up to 20 wt%. The synthesis strategy is universal that a variety of metal ions can be also used to form X–GR, and X–MC (X = Ti, V, Cr, Mn, Fe, Co, Ni, Cu or Zn) with similar stacked structure. Moreover, bimetallic polymer such as FeCo–GR can also be obtained by one-pot reaction and pyrolyzed into N doped mesoporous carbon (FeCo–MCN) under the mixture of N_2 and NH_3. FeCo–MCN-900 exhibits outstanding catalytic activity and excellent stability compared to those of the commercial Pt/C catalysts in oxygen reduction reaction (ORR).

2. Experimental section

2.1 Chemicals and materials

Gallic acid (GA), iron(III) chloride hexahydrate ($FeCl_3 \cdot 6H_2O$), cobalt(II) chloride hexahydrate ($CoCl_2 \cdot 6H_2O$), nickel(II) chloride hexahydrate ($NiCl_2 \cdot 6H_2O$), copper(II) chloride dihydrate ($CuCl_2 \cdot 2H_2O$), zinc chloride ($ZnCl_2$), titanium(III) chloride solution ($TiCl_3$, 20 wt% in H_2O), vanadium(III) chloride (VCl_3), chromium(III) chloride hexahydrate ($CrCl_3 \cdot 6H_2O$), and manganese(II) chloride tetrahydrate ($MnCl_2 \cdot 4H_2O$) were purchased from Aladdin. Ammonia (27 wt% aqueous solution), and ethanol were purchased from Beijing Chemical Works. All the chemicals were used without further purification.

2.2 Synthesis of X–GR

For a typical synthesis of Fe–GR, 0.81 g of GA, 19.8 mL of water and 8.4 mL of EtOH were combined and stirred to form a clear solution at 40 °C. Then, 0.9 mL of $FeCl_3$ solution (0.64 g mL^{-1}) was added under stirring. The colour of solution changed from colourless to dark blue immediately, and 1.2 mL of ammonia (~28 wt%) was added in the solution 30 minutes later. After 4 h, 0.9 mL of formaldehyde (~35 wt%) was added, and the solution was kept at 40 °C under stirring for 6 h. The product was collected by centrifugation, washed with ethanol for several times, and dried under ambient temperature.

X–GR with other metal was synthesized under the similar condition as Fe–GR.

2.3 Synthesis of FeCo–GR

0.81 g of GA, 19.8 mL of water and 8.4 mL of EtOH were combined and stirred to form a clear solution at 40 °C. Then, 0.5 mL of $FeCl_3$ solution (0.64 g mL^{-1}) and 0.4 mL of $CoCl_2$ solution (0.64 g mL^{-1}) was added under stirring. The color of solution changed from colorless to dark blue immediately, and 1.2 mL of ammonia (~28 wt%) was added in the solution 30 minutes later. After 4 h, 0.9 mL of formaldehyde (~35 wt%) was added, and the solution was kept at 40 °C under stirring for 6 h. The product was collected by centrifugation, washed with ethanol for several times, and dried under ambient temperature.

2.4 Synthesis of X–MC and X–MCN

As for X–MC-600, the obtained X–GR were heated under a nitrogen atmosphere at 2 °C min^{-1} from room temperature to 150 °C and kept at 150 °C for 2 h. The temperature was then raised at 5 °C min^{-1} to 600 °C and kept at 600 °C for 1 h. X–MC-700, X–MC-800, X–MC-900, and X–MC-1000 were obtained by changing the final temperature to 700, 800, 900, and 1000 °C. The synthesis of X–MCN had the same heating steps as X–MC but changed N_2 to the mixture of N_2 and NH_3.

2.5 Material characterization

The structure and morphology of X–GR and X–MC were analyzed with an FEI Tecnai G^2 F20 s-twin D573 field emission transmission electron microscope at an acceleration voltage of 200 kV and a JEOL JSM-6700F field-emission scanning electron microscope operated at 5 kV. The thermal gravimetric analyses (TG) were performed on a TGA Q500 thermogravimetric analyzer used in N_2 with a heating rate of 10 °C min^{-1}. N_2 adsorption–desorption isotherms were obtained at −196 °C on a Quantachrome NovaWin 4200e instrument. Samples were degassed at 150 °C for a minimum of 6 h prior to analysis. Raman spectra of Fe–MC-*x* was performed on a Renishaw inVia Raman microscope. Powder X-ray diffraction (XRD) patterns were collected by using a Rigaku 2550 diffractometer with Cu Kα radiation (λ = 1.5418 Å). The X-ray photoelectron spectroscopy (XPS) measurements were performed on a ESCALAB250 system with Al Kα radiation (1486.6 eV). The metal contents were quantitatively analysed by X-ray fluorescence (XRF) using a PANalytical AXIOS XRF spectrometer. Infrared (IR) spectra were recorded within the 400–4000 cm^{-1} region using a Bruker IFS 66 V/S FTIR spectrometer with KBr pellets.

2.6 Electrochemical measurements

Electrocatalytic activities for ORR of the as-prepared catalysts were evaluated on a CHI-660E electrochemical analyser. A three-electrode cell was used, consisting of a glass carbon RDE (5 mm in diameter, RRDE) as working electrode, an Hg/HgO, NaOH (1 M) electrode as the reference electrode, and a Pt wire electrode as the counter electrode. The electrolytes were 0.1 M KOH solution. The potential was scan between −0.70 and +0.30 V (*vs.* Hg/HgO) at a scan rate of 50 mV s^{-1} for CV at the ambient temperature after purging O_2 or N_2 gas for 30 min. All the working electrodes were prepared as following: 5 mg of catalysts and 20 μL of Nafion solution (5 wt%) were dispersed in 500 μL of EtOH by sonication to form a homogeneous ink. Then, 10 μL of ink was loaded onto polished glassy carbon rotating disk electrode of 0.196 cm^2 surface, and the electrode was dried at room temperature. The loading amount of catalysts on the electrode was about 0.5 mg cm^{-2}. For the RDE recording, the working electrode was scanned from +0.30 to −0.70 V at a rate of 10 mV s^{-1} with varying rotating speed from 400 rpm to 2500 rpm. Commercial 20 wt% Pt/C catalysts obtained from Alfa Aesar were used for comparison. The calibration of Hg/HgO reference electrode is performed in a standard three-electrode system with polished Pt wires as the working and counter electrodes, and the Hg/HgO electrode as the reference electrode. Electrolytes are pre-purged and saturated with high purity H_2. Linear scanning voltammetry (LSV) is then run at a scan rate of 0.1 mV s^{-1}, and the potential at which the current crossed zero is taken to be the thermodynamic potential (*vs.* Hg/HgO) for the hydrogen electrode reactions. In 0.1 M KOH, the zero-current point is at −0.900 V, so E (RHE) = E (*vs.* Hg/HgO) + 0.900 V.

The Koutecky–Levich plots (J^{-1} *vs.* $\omega^{-1/2}$) were analyzed at various electrode potentials. The slopes of the linear lines were used to calculate the number of electrons transferred (n) according to the following Koutecky–Levich equation.

$$\frac{1}{J} = \frac{1}{J_L} + \frac{1}{J_K} = \frac{1}{B\omega^{1/2}} + \frac{1}{J_K} \quad (1)$$

$$B = 0.62nFC_0(D_0)^{2/3}\nu^{-1/6} \quad (2)$$

$$J_K = nFkC_0 \quad (3)$$

where J is the measured current density; J_L is the diffusion-limiting current densities; J_K is the kinetic current density. ω is the angular velocity of the disk, n is the electrons transferred number, F is the Faraday constant (=96 485 C mol^{-1}), C_0 is the bulk concentration of O_2 (1.2×10^{-3} mol L^{-1} in 0.1 M KOH), D_0 is diffusion coefficient of O_2 (1.9×10^{-5} cm s^{-1} in 0.1 M KOH), ν is the kinematic viscosity of the electrolyte (0.01 cm^2 s^{-1} in 0.1 M KOH). k is the electron transfer rate constant. The number of electrons transferred (n) and J_K are obtained from the slope and intercept of the K–L plots. The durability test was carried out by means of the chronopotentiometry method for 20 000 s at 0.5 V (*vs.* RHE).

As for RRDE measurements, the Pt ring electrode of the RRDE was polarized at 1.25 V to oxidize HO_2^- intermediate from the disk electrode. The n values were verified according to the following equations.

$$n = 4|I_d|/(|I_d| + I_r/N) \quad (4)$$

where I_d is the disk current as obtained from the disk electrode, I_r is the oxidation current as measured on the Pt ring, N is the collection efficiency with a value of 0.41.

3. Results and discussion

GA is not only a low-cost environmentally friendly drug but also an excellent ligand because it has five available oxygen atoms—a carboxyl group and three phenolic oxygens that can chelate to metal ions with various coordination modes.[46] Iron gallate solution has been well known as an ink or a dye since antiquity. Thus, we typically choose Fe^{III} and GA to obtain Fe–GA nanoparticles *via* a convenient expanded Stöber method. Water, alcohol, and iron gallate can form emulsion droplets through the hydrogen bonding. Ammonia solution was used to adjust the pH of the solution. Fe–GA nanoparticles precipitated in the emulsion droplets and grew to be nanospheres at pH = 9 (Fig. 1b). However, Fe–GA nanospheres will fuse together without mother liquor because the coordinate bonds were not stable enough (Fig. S1c, ESI†). Thus, formaldehyde was chosen to stabilize Fe–GA nanospheres by forming polymer networks (Fe–GR) similar to resorcinol/formaldehyde resins. The SEM image of Fe–GR shows stacked sphere structure originating from fixed Fe–GA nanospheres (Fig. 1c). Fe–GR was carbonized under nitrogen atmosphere. The pyrolysis product of Fe–GR is denoted as Fe–MC-x, where x is the calcination temperature (in °C). Fe–MC-600 showed hollow structure in the TEM image (Fig. 1e), because the inner cores were not as stable as the crosslinked shell during the pyrolysis step. The mesopores about 10 nm (Fig. 1f) are mainly attributed to metal accumulation and transfer during the pyrolysis process.[47] Fe–MC-600 began to show layered graphitization structure in HRTEM image, because the high content of Fe can be used as efficient catalyst to accelerate graphitization in Fe–GR. The Fe content of Fe–MC were calculated to be as high as 20 wt% by X-Ray Fluorescence Spectrometer (XRF). To verify the universality of the method, other metals such as Ti, V, Cr, Mn, Co, Ni, Cu, and Zn were also used to fabricate X–GR with high yield more than 10 g from 250 mL of the reaction solution (Fig. 2a). SEM images show similar stacked structure in all these X–GRs (Fig. 2b, d and S2†) and TEM images of X–MC (Fig. 2c and e) show highly dispersed metal nanoparticles. By contrast, typical mesoporous carbon and commercial activated carbon with 10 wt% of the Fe content gave heavily agglomerated Fe_3O_4 particles after the same treatment as Fe–MC (Fig. S4†). Thus, the coordination–polymerization strategy has obvious advantages in the synthesis of graphitized mesoporous carbon with abundant dispersed metal nanoparticles.

The general coordination–polymerization–carbonization synthetic processes were preliminarily studied as below. For the coordination–polymerization processes, Fourier transform infrared (FTIR) spectroscopy was used to identify the changes of characteristic functional group in Fe–GA and Fe–GR. Compared to the spectra of GA (Fig. 3a), the stretching vibration and bending vibration peaks of phenolic hydroxyl O–H groups at

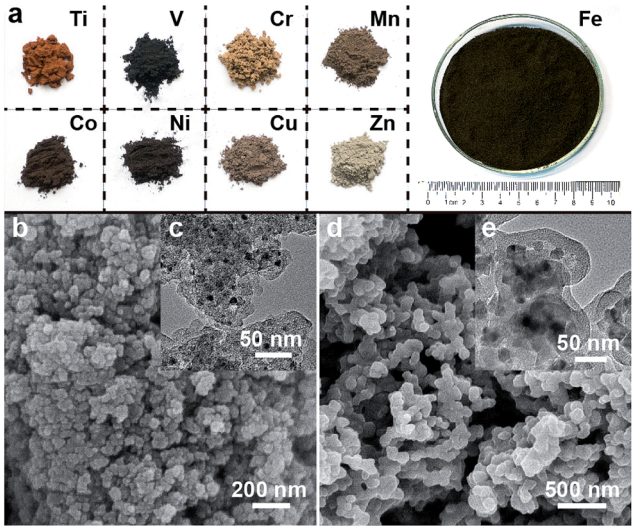

Fig. 2 (a) Photographs of X–GR with different metals; the quantity of Fe–GR powder in the glass dish is about 12 grams. SEM image (b) and TEM image (c) of V-MC. SEM image (d) and TEM image (e) of Cr–MC.

3496 cm^{-1} and 634 cm^{-1}, and carboxylic acid O–H group at 3280 cm^{-1} and 1425 cm^{-1} almost disappeared in the spectra of Fe–GA, indicating the formation of coordination bonds between Fe^{III} and GA.[48] The bending vibration peak of C–H group at 1446 cm^{-1} in the spectra of Fe–GR demonstrates the formation of the methylene group between benzene rings originated from cross-linking reaction. For the carbonization process, Fe–GR showed much better thermal stability with a higher carbonization yield of 40 wt% at 800 °C than that of Fe–GA (25 wt%), according to the thermogravimetry (TG) curves of Fe–GA and Fe–GR under N_2 atmosphere (Fig. 3b). The obvious weight loss of Fe–GA between 200 and 250 °C can be mainly attributed to the sublimation of GA. This weight loss process is not observed in the curve of Fe–GR, because GA was crosslinked and stabilized by formaldehyde. The pore characteristics of Fe–MC-*x* were examined by nitrogen adsorption experiment at 77 K (Fig. 4a). The nitrogen adsorption–desorption isotherms of Fe–GR-*x* exhibit characteristics of type IV indicating the mesoporous structure of the pyrolysis products. The Brunauer–Emmett–Teller surface areas (S_{BET}) of Fe–MC-600, Fe–MC-700, and Fe–MC-800, are 272, 255 and 235 $m^2\ g^{-1}$ based on the N_2 adsorption isotherm, respectively. Nonlinear Density Functional Theory (NLDFT) method was used to calculate the pore size distributions of Fe–GR-*x* (Fig. 4b). The mesopore distribution peaks at about 3 nm and 6 nm are mainly attributed to the thermal decomposition of Fe–GR, and metal accumulation and transfer during the pyrolysis process. X–MC-600 with various metals also showed similar porosity according to the nitrogen adsorption curves (Fig. S5†). Mesoporous carbon MC-600 without metal can be obtained after removing metal in Fe–MC-600 by acid, while the direct carbonization of GR can not obtain mesoporous carbon (Fig. S6†). Thus, the coordination process between metal ions and GA plays an important role in the formation of mesoporous carbon. The powder X-ray diffraction (XRD) patterns were used to confirm the formation of crystalline phase in Fe–MC-*x*. The peaks in XRD pattern of Fe–MC-*x* (Fig. 4c) are mainly matched with the diffraction peaks of Fe_3C (PDF 35-0772) and graphite-2H (PDF 41-1487). No peaks of iron oxide are found according to the XRD analysis, which is owing to the reductive atmosphere during heat treatment. The

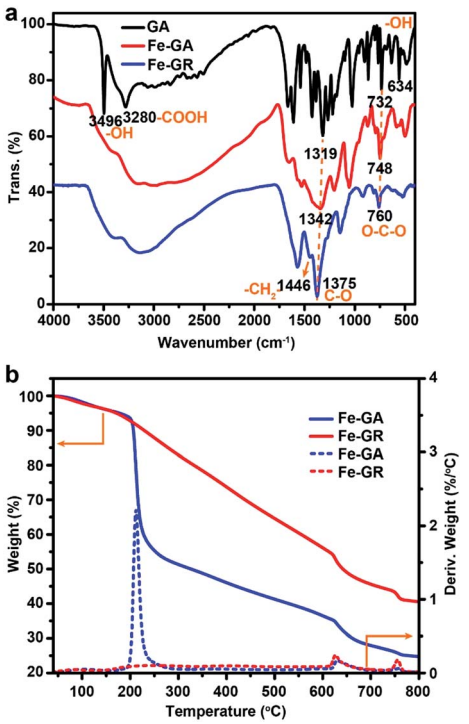

Fig. 3 (a) FTIR spectra of GA, Fe–GA and Fe–GR. (b) TG curves of Fe–GA and Fe–GR under N_2.

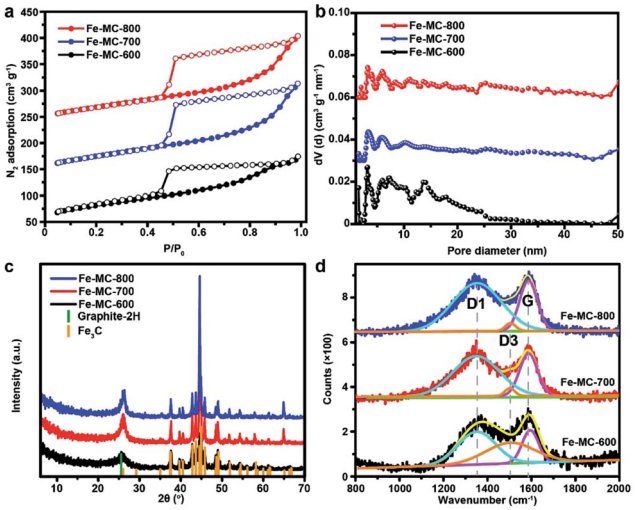

Fig. 4 (a) N_2 adsorption–desorption isotherms of Fe–MC-*x* at 77 K; the Fe–MC-700, and Fe–MC-800 curves are shifted on the vertical axis by 100, and 200 $cm^3\ g^{-1}$ for clarity. (b) Pore size distribution analysis for Fe–MC-*x* according to NLDFT model; the Fe–MC-700, and Fe–MC-800 curves are shifted on the vertical axis by 0.03, and 0.06 $cm^3\ nm^{-1}\ g^{-1}$ for clarity. (c) XRD patterns of Fe–MC-*x*. (d) Raman spectra of Fe–MC-*x*.

Raman spectra of Fe–GR-*x* (Fig. 4d) can be fit into three peaks: *ca.* 1350 cm^{-1} (D1 band) arising from the defects in graphitic lattice, *ca.* 1590 cm^{-1} (G band) arising from the in-plane vibration of the sp^2 carbon network and *ca.* 1500 cm^{-1} (D3 band) arising from amorphous carbon.[49] The D1/G band ratio almost do not change at different calcination temperature. The D3/G band ratio drastically decreases from 1.96 to 0.08 with the increase of calcination temperature, indicating the increase of the graphitization degree of Fe–MC-*x*.

Transition metals Fe and/or Co loaded on N doped carbon catalyst containing the critical site pyridyl-metal have been reported as efficient catalysts for ORR.[42,50] Taking advantage of the versatility of our fabrication method, we can conveniently one-pot synthesize bimetallic polymer FeCo–GR as the precursor of bimetallic catalyst. The precursor FeCo–GR, Fe–GR, and Co–GR was carbonized in the gas mixture of N_2 and NH_3 to obtain N doped catalyst FeCo–MCN, Fe–MCN, and Co–MCN. The electrocatalytic activities of FeCo–MCN-900, Fe–MCN-900 and Co–MCN-900 for ORR were initially investigated by cyclic voltammetry (CV) in 0.1 M KOH solution. In a nitrogen-saturated solution, the CV curves within the entire potential range showed no obvious reduction peaks for the cathodic current (Fig. 5d). In contrast, catalysts displayed well-defined cathodic peaks in the solution saturated with O_2. The oxygen reduction peak potential of FeCo–MCN-900 was more positive (0.81 V *versus* the reversible hydrogen electrode, RHE) than that of Fe–MCN-900 (0.61 V) and Co–MCN-900 (0.75 V), indicating enhanced ORR catalytic activity of bimetallic catalyst. Linear-sweep voltammetry (LSV) was carried out on rotating disk electrode (RDE) in O_2 saturated 0.1 M KOH at a scan rate of 10 mV s^{-1} to gain further insight into the ORR process for the electrodes. The RDE LSV curves (Fig. 4e) demonstrated clear enhancement of FeCo–MCN-900 based on several important indicators: the onset potential (E_{onset}), half-wave potential ($E_{1/2}$) and diffusion limiting current density (j_L). To verify the optimum calcination temperature, FeCo–GR was carbonized in the gas mixture of N_2 and NH_3 at different final temperature to obtain FeCo–MCN-*x*. As shown in Fig. 5e, $E_{1/2}$ of FeCo–MCN-900 (0.83 V) were the most positive among FeCo–MCN-*x*, and were comparable to that of commercial Pt/C catalyst (0.84 V, Fig. 4b).

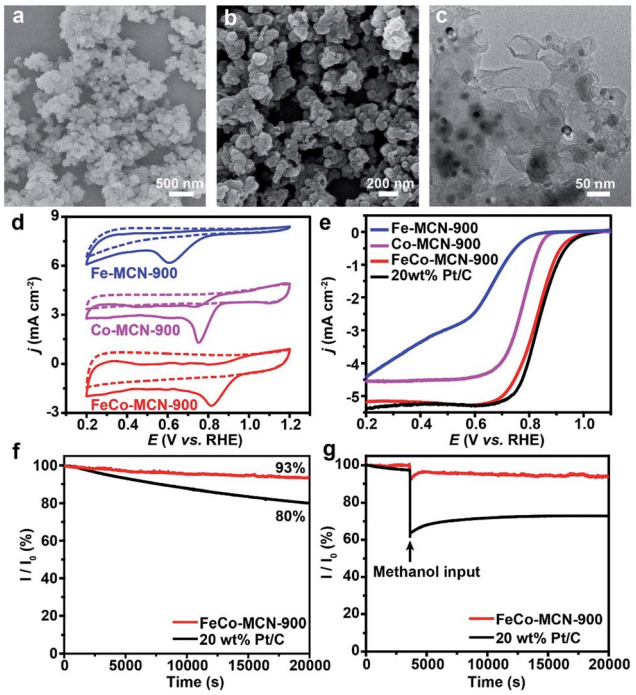

Fig. 5 (a) SEM image of FeCo–GR. (b) SEM image of FeCo–MCN-900. (c) TEM image of FeCo–MCN-900. (d) CV curves of X–MCN-900 in N_2-saturated and O_2-saturated 0.1 M KOH solution with a sweep rate of 50 mV s^{-1}. (e) LSV curves of X–MCN-900 in O_2-saturated 0.1 M KOH solution with a sweep rate of 10 mV s^{-1}. (f) Chronoamperometric responses of FeCo–MCN-900 and 20 wt% Pt/C catalysts in O_2-saturated 0.1 M KOH at 0.5 V. (g) Chronoamperometric responses of FeCo–MCN-900 and 20 wt% Pt/C catalysts showing the effect of adding 4 mL of methanol into the 100 mL of O_2-saturated 0.1 m KOH solution at 0.5 V.

To shed light on the kinetics of electrochemical catalytic ORR, Koutecky–Levich (K–L) plots derived from the LSV curves of FeCo–MCN-900 for ORR at various rotation speeds were obtained at the potential range of the diffusion-controlled region (Fig. S9a†). The inverse current density and the inverse square root of the rotational speed (j^{-1} *vs.* $\omega^{-1/2}$) showed good linear relationships and parallelism (Fig. S9b†), indicating first-order reaction kinetics with respect to the dissolved O_2. The average electron transfer number (n) was calculated to be 4.2 in the potential range between 0.2 and 0.6 V derived from the K–L plots, suggesting that FeCo–MCN-900 favors a 4e oxygen reduction process similar to that by Pt/C. The number of electrons transferred is 3.97 over the potential range of 0–0.8 V according to the results of RRDE (Fig. S10†), which is in agree with the results of RDE in Fig. S9.† Moreover, the stability of FeCo–MCN-900 and Pt/C catalyst is investigated at 0.5 V in O_2-saturated 0.1 M KOH solution at a rotation speed of 1600 rpm. During the period of 20 000 s, the current density of FeCo–MCN-900 remained 93%, whereas the Pt/C catalyst shows a much higher current loss of 20% (Fig. 5f). Furthermore, the methanol tolerant ability of FeCo–MCN-900 and Pt/C catalyst in 0.1 m KOH electrolyte was compared at the potential of 0.5 V in O_2-saturated 0.1 M KOH solution at a rotation speed of 1600 rpm. As shown in Fig. 5g, Pt/C catalyst suffered an instant drop in current upon the introduction of methanol into the electrolyte, while the current of the electrolyte with FeCo–MCN-900 remain almost unchanged. Thus, FeCo–MCN-900 possess better stability and far better resistance to methanol crossover than commercial Pt/C catalyst.

Several essential characterizations were performed to explore the nature of FeCo–MCN-900 catalyst. The TEM image of FeCo–MCN-900 (Fig. 5c) shows dispersed metal nanoparticles encapsulated in graphited porous carbon. The formation of crystalline phase in FeCo–MCN-900 was confirmed by XRD patterns (Fig. 6a). The peaks in XRD pattern of FeCo–MCN-900 are mainly matched with the diffraction peaks of Fe_3N (PDF 49-1662), Co_3Fe_7 alloy (PDF 48-1816) and graphite-2H (PDF 41-1487). According to XPS of FeCo–MCN-900 (Fig. S9†), the high-resolution C 1s peak was fitted into several peaks corresponding to Fe–C bond at 283.0 eV, C=C bond at 284.8 eV, and C–N bond at 286.0 eV, indicating the incorporation of nitrogen

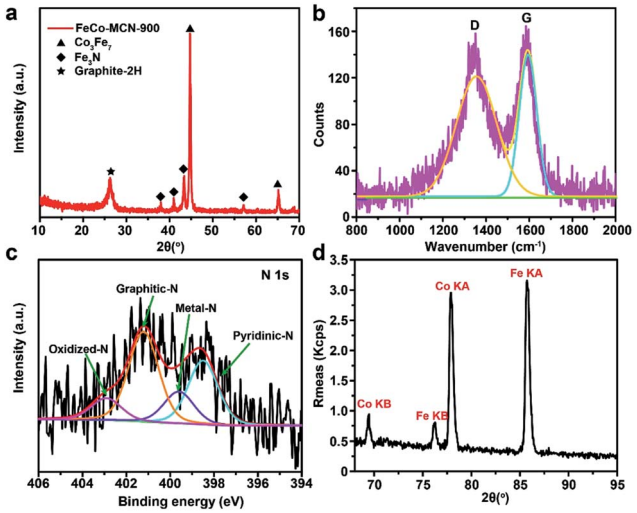

Fig. 6 Characterizations of FeCo–MCN-900. (a) XRD pattern. (b) Raman spectra. (c) N 1s XPS spectra. (d) XRF spectra.

into the graphitic basal plane.[19] High-resolution XPS N 1s spectra (Fig. 6c) demonstrates four types of nitrogen atoms and the peaks located at 398.5, 399.6, 401.2 and 402.9 eV in a percentage of 30.8, 15.3, 43.4 and 10.5%, related to the pyridinic N, metal N, graphitic N and oxidized N, respectively.[51] The N content reached 2.0 at% in FeCo–MCN-900 and pyridinic N content constituted 30.8% of the total nitrogen content, suggesting effective enrichment of pyridinic N in FeCo–MCN-900 *via* thermal treatment in NH_3. The Fe and Co content in FeCo–MCN-900 are calculated to be about 14 and 13 wt% by XRF (Fig. 6d), respectively. However, the Fe and Co 2p peaks were very weak in XPS spectra (Fig. S11†) and fitted into several peaks corresponding to Fe^{III} and Co^{II}, suggesting that Co_3Fe_7 was entirely encapsulated by carbon shells. The encapsulated Co_3Fe_7 alloy NPs can activate the surrounding graphitic layers, which also act as active sites towards the ORR.[52] Considering all the above, the excellent electrocatalytic activities and stability of FeCo–MCN-900 can originate from the porous structure and critical sites, including abundant pyridinic N, graphited carbon coated Fe_3N and Co_3Fe_7 alloy.[53] Some controlled trials, such as Fe–MCN-900, Co–MCN-900, Fe–MC-600 and FeCo–MC-600 containing part of the catalytic activity sites in FeCo–MCN-900, also exhibited certain activity, but not as well as FeCo–MCN-900 (Fig. 5 and S8†). Thus, these catalytic sties of FeCo–MCN-900 sample, such as Fe–N–C, Co–N–C, N–C, metal nitrides and metal carbides, possibly work together by a synergetic effect in ORR and lead to the excellent performance of FeCo–MCN-900.

4. Conclusions

In conclusion, we have demonstrated the general coordination–polymerization strategy using formaldehyde to crosslink coordination nanospheres to synthesize a series of polymers and mesoporous carbons with abundant dispersed metal nanoparticles. Various transition metal such as Ti, V, Cr, Mn, Fe, Co, Ni, Cu, and Zn can be used to fabricate X–GR and X–MC with similar stacked structure. Furthermore, the general strategy can be expanded to the fabrication of bimetallic catalyst FeCo–MCN-900, which possesses comparable ORR catalytic activity, better stability and far better resistance to methanol crossover compared to those of commercial Pt/C catalyst. Obviously, the applications of X-MC are not limited to ORR, and still worth for deeper research. The design concept presented here is expected to stabilize more fragile coordination complexes and prepare a series of heterometal catalysts.

Conflicts of interest

There are no conflicts to declare.

Acknowledgements

This work was supported by the Young Thousand Talented Program and the National Natural Science Foundation of China (No. 21671073, 21621001, 21671074, 21371067 and 21373095), and the "111" Project of the Ministry of Education of China (B17020).

Notes and references

1 A. S. Aricò, P. Bruce, B. Scrosati, J. M. Tarascon and S. W. Van, *Nat. Mater.*, 2005, **4**, 366–377.
2 X. Lu and C. Zhao, *Nat. Commun.*, 2015, **6**, 6616.
3 M. K. Debe, *Nature*, 2012, **486**, 43–51.
4 X. Zhou, J. Qiao, Y. Lin and J. Zhang, *Adv. Energy Mater.*, 2014, **4**, 1289–1295.
5 M. Shao, Q. Chang, J. P. Dodelet and R. Chenitz, *Chem. Rev.*, 2016, **116**, 3594–3657.
6 C. Chen, Y. Kang, Z. Huo, Z. Zhu, W. Huang, H. L. Xin, J. D. Snyder, D. Li, J. A. Herron and M. Mavrikakis, *Science*, 2014, **343**, 1339–1343.
7 Y. Li, W. Zhou, H. Wang, L. Xie, Y. Liang, F. Wei, J. C. Idrobo, S. J. Pennycook and H. Dai, *Nat. Nanotechnol.*, 2012, **7**, 394–400.
8 I. E. L. Stephens, J. Rossmeisl and I. Chorkendorff, *Science*, 2016, **354**, 1378–1379.
9 L. Bu, N. Zhang, S. Guo, X. Zhang, J. Li, J. Yao, T. Wu, G. Lu, J. Y. Ma and D. Su, *Science*, 2016, **354**, 1410–1414.
10 M. Li, Z. Zhao, T. Cheng, A. Fortunelli, C. Y. Chen, R. Yu, Q. Zhang, L. Gu, B. Merinov and Z. Lin, *Science*, 2016, **354**, 1414–1419.
11 J. Snyder, K. Livi and J. Erlebacher, *Adv. Funct. Mater.*, 2013, **23**, 5494–5501.
12 M. Justus, X. Wei, M. Martin and S. Wolfgang, *Angew. Chem., Int. Ed.*, 2015, **54**, 10102–10120.
13 R. Bashyam and P. Zelenay, *Nature*, 2006, **443**, 63–66.
14 X. Tian, J. Luo, H. Nan, Z. Fu, J. Zeng and S. Liao, *J. Mater. Chem. A*, 2015, **3**, 16801–16809.
15 G. Jiang, H. Zhu, X. Zhang, B. Shen, L. Wu, S. Zhang, G. Lu, Z. Wu and S. Sun, *ACS Nano*, 2015, **9**, 11014–11022.
16 L.-B. Lv, T.-N. Ye, L.-H. Gong, K.-X. Wang, J. Su, X.-H. Li and J.-S. Chen, *Chem. Mater.*, 2015, **27**, 544–549.

17 S. Guo, S. Zhang and S. Sun, *Angew. Chem., Int. Ed.*, 2013, **52**, 8526–8544.
18 J. Shui, M. Wang, F. Du and L. Dai, *Sci. Adv.*, 2015, **1**, e1400129.
19 Z. Lin, G. Waller, Y. Liu, M. Liu and C. P. Wong, *Adv. Energy Mater.*, 2012, **2**, 884–888.
20 J. X. Feng, H. Xu, Y. T. Dong, S. H. Ye, Y. X. Tong and G. R. Li, *Angew. Chem., Int. Ed.*, 2016, **55**, 3694–3698.
21 Y. C. Wang, Y. J. Lai, S. Lin, Z. Y. Zhou, J. G. Liu, W. Qiang, X. D. Yang, C. Chi, S. Wei and Y. P. Zheng, *Angew. Chem., Int. Ed.*, 2015, **54**, 9907–9910.
22 P. Yin, T. Yao, Y. Wu, L. Zheng, Y. Lin, W. Liu, H. Ju, J. Zhu, X. Hong and Z. Deng, *Angew. Chem., Int. Ed.*, 2016, **55**, 10800–10805.
23 U. I. Kramm, I. Herrmanngeppert, J. Behrends, K. Lips, S. Fiechter and P. Bogdanoff, *J. Am. Chem. Soc.*, 2015, **138**, 635–640.
24 R. J. White, K. Tauer, M. Antonietti and M.-M. Titirici, *J. Am. Chem. Soc.*, 2010, **132**, 17360–17363.
25 D. Higgins, F. M. Hassan, H. S. Min, J. Y. Choi, M. A. Hoque, U. L. Dong and Z. Chen, *J. Mater. Chem. A*, 2015, **3**, 6340–6350.
26 M. Lefèvre, E. Proietti, F. Jaouen and J. P. Dodelet, *Science*, 2009, **324**, 71–74.
27 K. Ai, Y. Liu, C. Ruan, L. Lu and G. M. Lu, *Adv. Mater.*, 2013, **25**, 998–1003.
28 H. Xue, J. Tang, H. Gong, H. Guo, X. Fan, T. Wang, J. He and Y. Yamauchi, *ACS Appl. Mater. Interfaces*, 2016, **8**, 20766–20771.
29 H. Gong, H. Xue, T. Wang, H. Guo, X. Fan, L. Song, W. Xia and J. He, *ACS Appl. Mater. Interfaces*, 2016, **8**, 18060–18068.
30 L. Song, T. Wang, Y. Ma, H. Xue, H. Guo, X. Fan, W. Xia, H. Gong and J. He, *Chem.–Eur. J.*, 2017, **23**, 3398–3405.
31 X. Cui, S. Yang, X. Yan, J. Leng, S. Shuang, P. M. Ajayan and Z. Zhang, *Adv. Funct. Mater.*, 2016, **26**, 5708–5717.
32 Y. Wan, Y. Shi and D. Zhao, *Chem. Mater.*, 2007, **20**, 932–945.
33 H. Bi, T. Lin, F. Xu, Y. Tang, Z. Liu and F. Huang, *Nano Lett.*, 2016, **16**, 349–354.
34 Y. Zhang, S. Wei, F. Liu, Y. Du, S. Liu, Y. Ji, T. Yokoi, T. Tatsumi and F. S. Xiao, *Nano Today*, 2009, **4**, 135–142.
35 Y. Niu, X. Huang, X. Wu, L. Zhao, W. Hu and C. Ming Li, *Nanoscale*, 2017, **9**, 10233–10239.
36 Y. Z. Chen, C. Wang, Z. Y. Wu, Y. Xiong, Q. Xu, S. H. Yu and H. L. Jiang, *Adv. Mater.*, 2015, **27**, 5010–5016.
37 M. Hu, Y. Ju, K. Liang, T. Suma, J. Cui and F. Caruso, *Adv. Funct. Mater.*, 2016, **26**, 5827–5834.
38 Q. Lin, X. Bu, A. Kong, C. Mao, F. Bu and P. Feng, *Adv. Mater.*, 2015, **27**, 3431–3436.
39 L. Li, C. Yuan, D. Zhou, A. E. Ribbe, K. R. Kittilstved and S. Thayumanavan, *Angew. Chem., Int. Ed.*, 2015, **54**, 12991–12995.
40 J. Wei, Y. Liang, Y. Hu, B. Kong, J. Zhang, Q. Gu, Y. Tong, X. Wang, S. P. Jiang and H. Wang, *Angew. Chem., Int. Ed.*, 2016, **55**, 12470–12474.
41 M. A. Rahim, K. Kempe, M. Müllner, H. Ejima, Y. Ju, M. P. V. Koeverden, T. Suma, J. A. Braunger, M. G. Leeming and B. F. Abrahams, *Chem. Mater.*, 2015, **27**, 5825–5832.
42 B. Wurster, D. Grumelli, D. Hötger, R. Gutzler and K. Kern, *J. Am. Chem. Soc.*, 2016, **138**, 3623–3626.
43 K. Strickland, E. Miner, Q. Jia, U. Tylus, N. Ramaswamy, W. Liang, M. T. Sougrati, F. Jaouen and S. Mukerjee, *Nat. Commun.*, 2015, **6**, 7343.
44 J. Wei, Y. Liang, Y. Hu, B. Kong, G. P. Simon, J. Zhang, S. P. Jiang and H. Wang, *Angew. Chem., Int. Ed.*, 2016, **55**, 1355–1359.
45 H. Ejima, J. J. Richardson, K. Liang, J. P. Best, M. P. van Koeverden, G. K. Such, J. Cui and F. Caruso, *Science*, 2013, **341**, 154–157.
46 R. K. Feller and A. K. Cheetham, *Solid State Sci.*, 2006, **8**, 1121–1125.
47 M. Zhao and H. Song, *J. Mater. Sci. Technol.*, 2011, **27**, 266.
48 L. L. Justino, I. Reva and R. Fausto, *J. Chem. Phys.*, 2016, **145**, 014304.
49 V. Perazzolo, C. Durante, R. Pilot, A. Paduano, J. Zheng, G. A. Rizzi, A. Martucci, G. Granozzi and A. Gennaro, *Carbon*, 2015, **95**, 949–963.
50 M. Sun, H. Liu, Y. Liu, J. Qu and J. Li, *Nanoscale*, 2015, **7**, 1250–1269.
51 X. Li, H. Wang, J. T. Robinson, H. Sanchez, G. Diankov and H. Dai, *J. Am. Chem. Soc.*, 2009, **131**, 15939–15944.
52 M. Li, T. Liu, L. Fan, X. Bo and L. Guo, *J. Alloys Compd.*, 2016, **686**, 467–478.
53 X. Huang, Z. Yang, B. Dong, Y. Wang, T. Tang and Y. Hou, *Nanoscale*, 2017, **9**, 8102–8106.